Mechanisms of austenite growth during intercritical annealing in medium manganese steels

Rama Srinivas Varanasi[1], Marta Lipińska-Chwałek[2,3], Joachim Mayer[2,3], Baptiste Gault[1,4], Dirk Ponge[1]

[1]Max-Planck-Institut für Eisenforschung GmbH, Max-Planck-Straβe 1, 40237, Düsseldorf, Germany

[2]Central Facility for Electron Microscopy (GFE), RWTH Aachen University, 52074 Aachen, Germany

[3]Ernst Ruska-Centre (ER-C) for Microscopy and Spectroscopy with Electrons, Forschungszentrum Jülich GmbH, 52425 Jülich, Germany

[4]Department of Materials, Royal School of Mines, Imperial College, Prince Consort Road, London SW7 2BP, United Kingdom.

Abstract

The third-generation advanced high strength medium manganese (3-12 wt. %) steels typically consist of ultrafine-grained dual-phase (austenite-ferrite) microstructure, obtained through the intercritical annealing of martensite at temperatures typically $\leq 0.5T_{melt}$, where the bulk diffusion of Mn is extremely slow. Yet, the manganese partitioning plays a prominent role in the austenite growth from the martensitic matrix during this annealing step. Therefore, the 'short circuit' diffusion paths provided by grain boundaries (GBs) and dislocations must be crucial to the austenite growth. However, this influence is not well understood across the literature. In the present work, we study the mechanisms of austenite growth in a cold-rolled intercritically annealed medium manganese steel of composition Fe-10Mn-0.05C-1.5Al (wt. %). We provide evidence of manganese transport to austenite through GB diffusion, GB migration and dislocation pipe diffusion. Furthermore, the influence of GB misorientation on austenite growth is also reported.

Graphical abstract

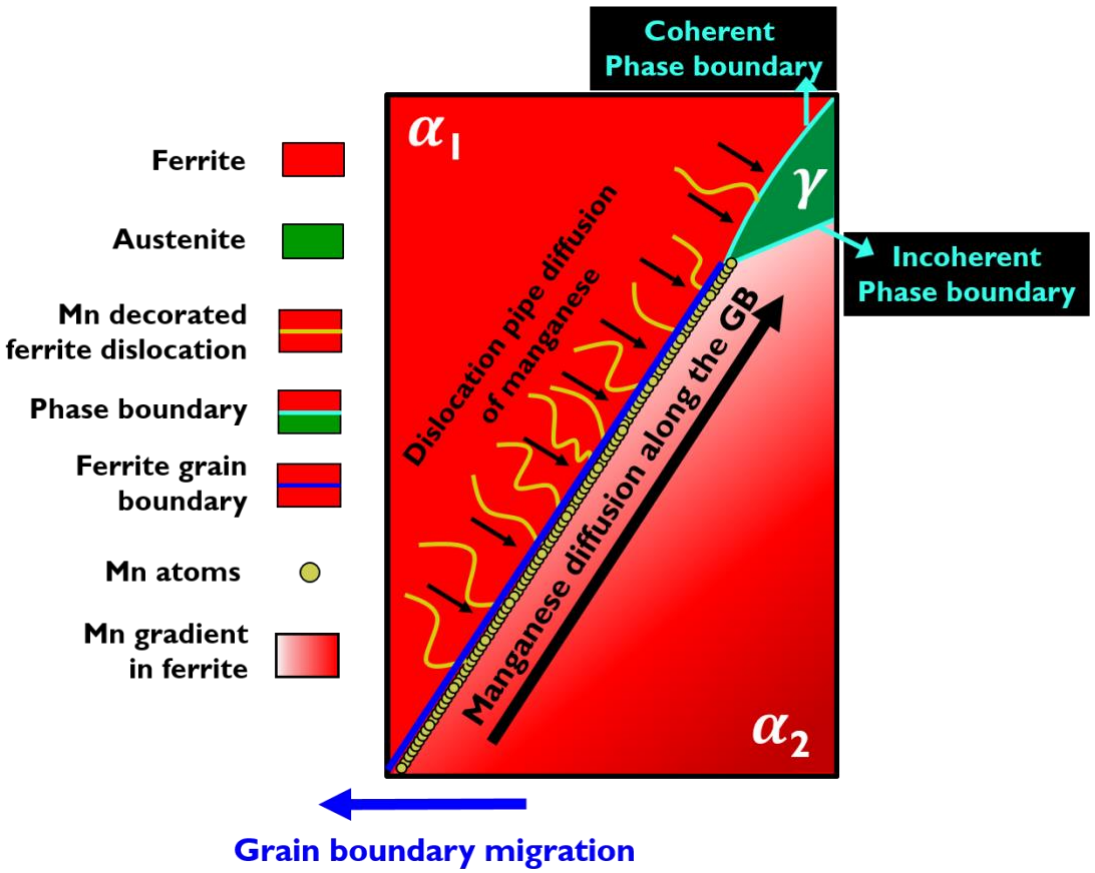

Key words:

Grain boundary diffusion, Atom probe tomography, Dual phase steels, Grain boundary migration, Pipe diffusion

It is well established that the grain boundaries (GBs) and dislocations provide fast diffusion paths ('short circuit' paths or the so called rapid diffusion paths) in materials [1-5]. These 'short circuit' paths are particularly relevant in the context of austenite growth during intercritical annealing in medium manganese steels (3-12 wt. % Mn). Studies [6-8] in the recent past have revealed manganese segregation to ferrite GBs as a pathway for austenite nucleation in intercritically annealed medium manganese steels. Austenite growth is achieved by the movement of the austenite-ferrite phase boundary towards the ferrite. At the interface boundary between the growing austenite and the ferrite, there exists a local equilibrium [9]. The partitioning of elements (such as manganese) between austenite and ferrite depends on the intercritical temperature. Typically, the equilibrium manganese concentration of austenite at the phase boundary is greater than that of ferrite. In other words, at the moving phase boundary, ferrite will be transformed to new reverted austenite with higher manganese concentration. Diffusion of manganese inside the ferrite is thus required to feed this transformation. However, no manganese diffusion is required inside the austenite. The kinetics of the austenite growth is therefore determined by the diffusion rate of manganese in ferrite [10, 11]. Since intercritical annealing temperatures are typically $\leq 0.5T_{melt}$, wherein even in the bcc ferrite the bulk diffusion is extremely slow, and thus the GBs and dislocations are expected to play a key role in solute transport [12, 13]. Yet, the role of these 'short circuit' paths in manganese transport for austenite growth is not well understood.

Earlier, Navara et al. [10] have reported GB diffusion and GB migration as a rapid manganese transport mechanism to the growing austenite. The authors used scanning transmission electron microscopy (STEM) and energy dispersive X-ray (EDX) spectroscopy for their studies. However, they pointed out that the use of atom probe would provide a more accurate understanding. Here, we aim to understand the mechanisms of austenite growth in medium manganese steel with the composition Fe-10Mn-0.05C-1.5Al (wt. %). The alloy was solution annealed at 1100°C for 3 hours and quenched. Subsequently, it was cold-rolled to achieve a 50% thickness reduction. The detailed alloy synthesis has been reported elsewhere [14]. The intercritically annealed specimen will be referred to as IAT/t, where T is the intercritical annealing temperature in °C and t is the intercritical annealing time in hours. In the current work ferrite refers to interrtically annealed recovered martensite.

Sample preparation for atom probe tomography (APT) [15] and transmission electron microscopy (TEM) [16] was carried out using a dual-beam FEI Helios NanoLab 660 scanning-electron microscope (SEM) - focused ion beam (FIB). APT investigations were conducted in a LEAP 5000XR

(Cameca Instrument, Inc. Madison, WI, USA), and the data was reconstructed using IVAS (3.8.4). The APT specimens were measured in laser pulsing mode at 60K with a repetition rate of 125 kHz and pulse energy of 40 pJ. Scanning transmission electron microscopy (STEM) with energy dispersive X- EDX spectral imaging was conducted in a high-resolution, Cs probe corrected FEI Titan G2 80–200 STEM [17]. Transmission Kikuchi diffraction (TKD) on the TEM lamella was performed in a Zeiss Merlin field emission gun scanning electron microscope (SEM) equipped with a Bruker-Nano EBSD detector. Phase fraction and Gibbs energy calculations were obtained using Thermo-calc (2017b)-TCFE9 database.

The cementite mole fraction estimated from Thermo-Calc in the medium manganese steel at 500°C is 4.7×10^{-4} (supplementary figure S1). Thus, an intercritical annealing temperature of 500°C (annealed for 6 hours) was initially selected to eliminate the cementite formation (IA500/6). Furthermore, for the IA500/6, the (ferrite) bulk manganese diffusion distance is significantly lower (~ 5nm) to aid austenite growth, as will be shown later. Consequently, for the IA500/6, austenite growth is expected to rely on 'short circuit' diffusion pathways.

To characterize austenite grains of the order of 10 nm, difficult to index by EBSD [18], we used transmission Kikuchi diffraction (TKD) [19]. Figure 1a-d illustrates the TKD data of the IA500/6, wherein austenite nucleation is observed both at the low angle grain boundaries (LAGBs) and high angle grain boundaries (HAGBs). The corresponding misorientations of the GBs (labeled in figure 1b, 1d) are shown in table 1. While the austenite formed at the LAGBs is ~10-30 nm in size, at HAGBs it can be as large as ~300 nm. It is observed that the austenite formed at the LAGBs is predominantly growing along the GB. While triple points (highlighted with a circle) appear devoid of austenite nucleation, it is important to note that the planar cross-section is observed in TKD and only the regions close to the bottom surface of the lamella can be mapped using TKD [20]. A possible austenite nucleation along a triple line going perpendicular into the lamella cannot be revealed with this measurement and, hence, cannot be excluded.

Boundary	Misorientation (°)
LAGB[i]	13.1
LAGB[ii]	8.5
HAGB[1]	55
HAGB[2]	60
HAGB[3]	50

Table 1: Misorientation of the grain boundaries indexed in figures 1b and 1d.

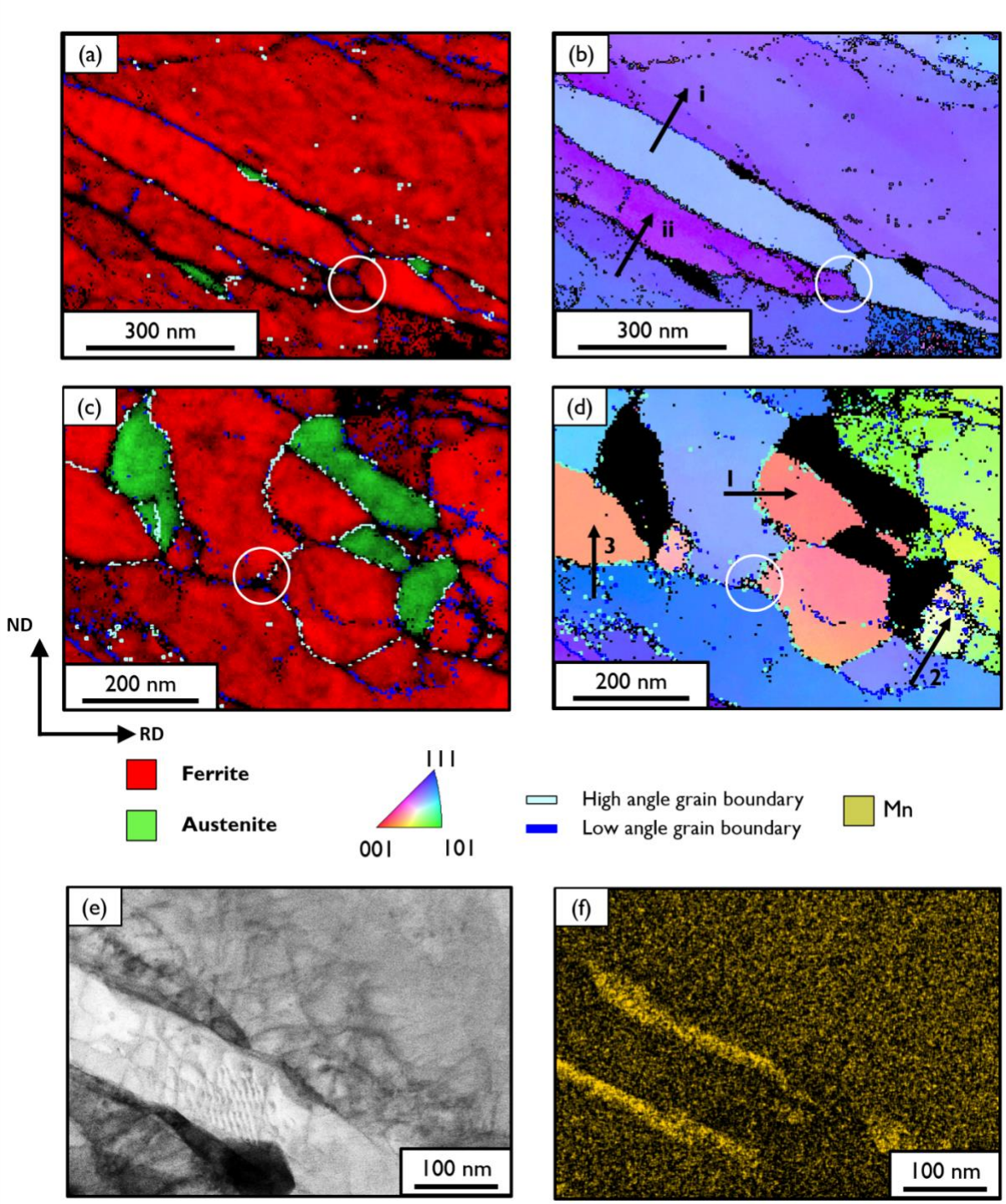

Figure 1 TKD studies of the IA500/6 steel. (a) Phase map indicating austenite nucleation at LAGBs. (b) IPF map corresponding to (a). (c) Phase map indicating austenite nucleation at HAGBs. (d) IPF map corresponding to (c). LAGBs are indicated in (b) with i and ii, while HAGBs are labeled in (d) with 1, 2, and 3. Corresponding misorientation angles of indicated GBs are given in table I. The white circles in (a-d) indicate triple junctions without austenite nucleation. (e) Bright-field STEM micrograph of the area indicated in (a) with white dotted rectangle. (f) EDX Mn distribution map corresponding to (f).

Figure 1f shows the EDX elemental distribution map of Mn for the area presented in STEM micrograph in figure 1e. The manganese-rich regions in figure 1f correspond to austenite growing along the ferrite GB. It is also important to note the dislocations terminating at the grain/phase boundary in the TEM image in figure 1e. The possibility of pipe diffusion of manganese along such dislocations is discussed later.

The local equilibrium at the phase boundary [9] ensures that the fresh austenite forms already with the equilibrium Mn concentration, thus, diffusion inside the FCC austenite is not required for the growth of austenite. For the ferrite, in addition to the bulk diffusion [21], dislocation pipe diffusion [22], GB diffusion [13], GB migration [10, 22] and recovery of dislocations (moving dislocation pipes) [22] aid the solute diffusion. Table 2 summarizes the diffusion coefficients of different diffusion pathways reported in the literature for ferrite (BCC) and austenite (FCC) at 500°C. A notation $\mathrm{D}_{\mathrm{M}}^{\mathrm{X}}$ has been used herein for the diffusion coefficient, where X stands for diffusing element (such as Mn, Fe or C), and M stands for the diffusion channel such as B for bulk, Dis for dislocation, and GB for grain boundary. Since the bulk diffusion of C in ferrite ($\mathrm{D}_{\mathrm{B-BCC}}^{\mathrm{C}}$ at 500°C is 10^{-12} m^2s^{-1} [23]) is orders of magnitude faster compared to the bulk diffusion of Mn in ferrite ($\mathrm{D}_{\mathrm{B-BCC}}^{\mathrm{Mn}}$ at 500°C is $\sim 10^{-21}$ m^2s^{-1} [21]), manganese diffusion in ferrite is considered to be the rate limiting factor for austenite growth.

Since GB and dislocation diffusion coefficients for Mn in ferrite at 500°C are not reported in the literature, for the need of our discussion we consider the corresponding self-diffusion coefficients of Fe, to provide us an approximation. In table 2 we calculate the diffusion distances for the annealing time of 6 hours at 500°C. Given that the bulk diffusion is three-dimensional, GB diffusion is two-dimensional and dislocation pipe diffusion is one-dimensional, the diffusion distance equation has been modified accordingly (table 2).

		Diffusion coefficient (m^2s^{-1})	Diffusion distance	
Bulk	$\mathbf{D^{C}_{B-BCC}}$ **[23]**	$\mathbf{\sim 10^{-12}}$	$\sqrt{6 * D^{Mn}_{B-BCC}t}$	360000 nm
	$\boldsymbol{D^{Mn}_{B-BCC}}$ **[21]**	$\mathbf{\sim 10^{-21}}$	$\sqrt{6 * D^{Mn}_{B-BCC}t}$	11.4 nm
	$\boldsymbol{D^{Mn}_{B-FCC}}$ **[24]**	$\mathbf{\sim 10^{-22}}$	$\sqrt{6 * D^{Mn}_{B-FCC}t}$	3.6 nm
	$\boldsymbol{D^{Fe}_{B-BCC}}$ **[25]**	$\mathbf{\sim 8 \times 10^{-23}}$	$\sqrt{6 * D^{Fe}_{B-BCC}t}$	3.2 nm
GB	$\boldsymbol{D^{Fe}_{GB-BCC}}$ **[3]**	$\mathbf{\sim 2 \times 10^{-15}}$ to $\mathbf{\sim 10^{-12}}$	$\sqrt{4 * D^{Fe}_{GB-BCC}t}$	13100 nm
Dislocation	$\boldsymbol{D^{Fe}_{Dis-BCC}}$ **[26]**	$\mathbf{\sim 10^{-17}}$	$\sqrt{2 * D^{Fe}_{Dis-BCC}t}$	656 nm

Table 2 Diffusion coefficients D^X_M for different pathways in ferrite (BCC) and austenite(FCC). X stands for diffusing element (such as Mn, Fe or C), and M indicates diffusion channel, such as bulk (B), dislocation (Dis), and grain boundary (GB). Diffusion coefficients correspond to the annealing temperature of 500°C. Diffusion distances are calculated for annealing time of 6 hours. The Mn bulk diffusion in austenite is slower when compared to the Mn bulk diffusion in ferrite.

The bulk Mn diffusion distance of 11.4 nm in ferrite (table 2), is significantly lower compared to the size of the austenite grains (~300 nm) observed for the IA500/6 (see e.g. figure 1c). Thus the bulk diffusion of manganese cannot meaningfully aid the process of austenite growth for the IA500/6. The GB diffusion is, therefore expected to be the dominant mass transport mechanism [12, 13]. It is important to note that the GB diffusion coefficient is dependent on the character of the GB [3, 27]. The $\mathrm{D^{Fe}_{GB-BCC}}$ was reported to vary up to by four orders of magnitude at 600°C for a Σ5 GB, depending on the GB misorientation (table 3 [3]). Given the dependence of diffusion coefficient on GB character, it is thus reasonable to conclude that at $D^{Mn}_{HAGB} > D^{Mn}_{LAGB}$ at 500°C in the ferrite. We have reported above (figure 1) that the austenite grain size at HAGB is significantly (~25 times) greater compared to the austenite at a LAGB for the IA500/6. The predominant GB diffusion at HAGB compared to LAGB, thus explains the preferential growth of austenite nucleated at the HAGBs compared to the austenite at the LAGBs for the IA500/6.

Grain boundary geometry	Misorientation (in °)	D^{Fe}_{GB-BCC} (in m^2s^{-1}) at 600°C
Σ5(310)	36.87	~10^{-15}
Σ5(730)	46.40	~10^{-13}
Σ5(210)	53.13	~10^{-11}

Table 3 GB diffusion coefficients for Σ5 GB for different GB misorientations. Values are taken from Starikov et al. [3], wherein D^{Fe}_{GB-BCC} was calculated using the embedded-atom method (EAM)-based potential developed by Chiesa et al. [28]

Given that the starting microstructure prior to intercritical annealing was a cold-rolled martensitic microstructure, the stored deformation energy provides a driving force for GB migration.

The velocity of a grain boundary v_{GB} is given by equation 1.

$$v_{GB} = mp \quad (1)$$

Wherein m, the mobility of a grain boundary is obtained from equation 2.

$$m = \frac{b^2 D_m}{kT} \quad (2)$$

k is the Boltzmann constant, b is the Burgers vector, T is the temperature, and D_m is the diffusion coefficient for jumps through the grain boundary.

p, the pressure on the GB due to stored deformation energy is given by

$$p = \rho \frac{Gb^2}{2} \quad (3)$$

The shear modulus *G* is assumed to be 100 GPa [29], ρ is the dislocation density. In BCC iron b = 2.48 Å. The dislocation density (ρ) was reported to be ~1 x 10^{16} m^{-2} in a 50% cold-rolled martensite [30].

GB segregation of manganese in ferrite causes solute drag during the GB migration [31, 32]. The motion of manganese solute atoms (moving behind the ferrite GB) can be considered here as the rate-determining process. Hence, the lower bound approximation for the velocity of a GB can be calculated by $D_m \cong D^{Mn}_{B-BCC}$ [31]. The velocity of GB (calculated from equation 1) reaches 1.7 x 10^{-4} nm/s and the distance of ferrite GB migration is 3.6 nm. However, the diffusion coefficient for jumps through the grain boundary, without the solute drag, can be significantly greater and hence the GB migration distance can also be significantly larger. It is also essential to note that the GB

migration rate depends on the GB character [32] and HAGBs were reported to show higher mobility compared to LAGBs [33].

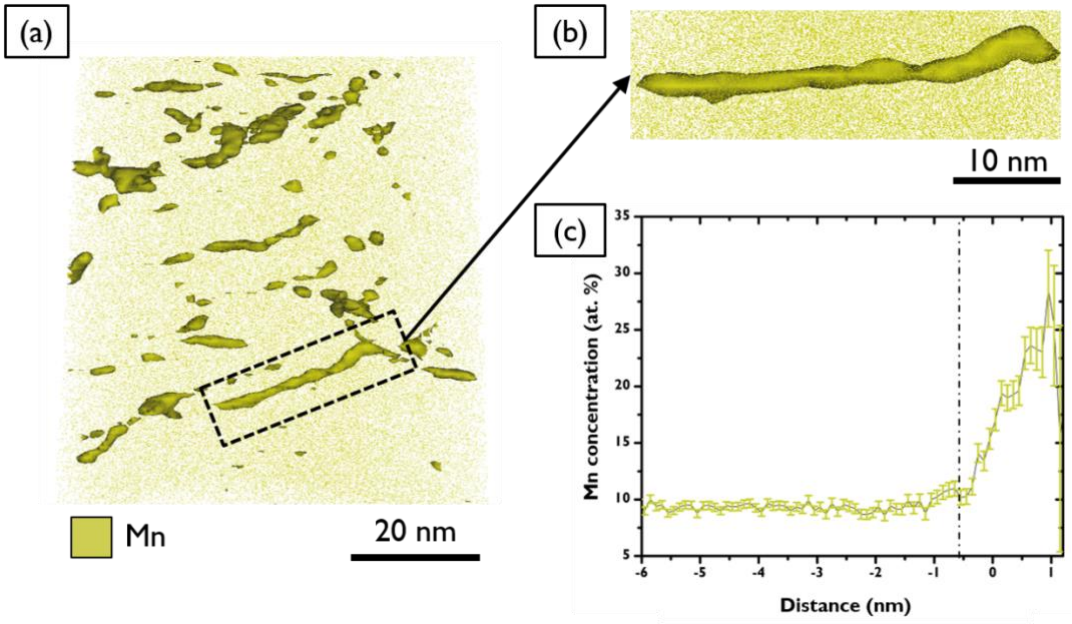

Figure 2 (a-b) APT measurement showing enrichment of dislocation with manganese for the IA500/6 steel. Mn-enrichment at the dislocation is highlighted by 14 at. % Mn iso-surface. (c) Proximal histogram [34] (or Proxigram) of the manganese segregation to the dislocation indicated in (b). 0 nm corresponds to 14 at. % Mn concentration. Positive distance corresponds to the enrichment at the dislocation wherein, while the negative distance indicates the bulk Mn concentration. To confirm the absence of any carbides at the dislocation, proxigram with carbon concentration is shown in supplementary figure S2.

Solute diffusion can occur via pipe-diffusion through dislocations [4, 5]. Kuzmina et al. [35] and Kwiatkowski da Silva et al. [36] reported manganese segregation to dislocations in a cold-rolled, intercritically annealed medium manganese steel. Our APT measurements revealed a similar manganese enrichment at dislocations for the IA500/6 (figure 2a-c), while STEM investigations (presented in Figure 1e) confirmed presence of dislocations termination at grain/phase boundaries. The schematic in figure 3 summarizes the two prominent diffusion paths relevant for the austenite growth, namely dislocations and GBs. If a dislocation terminates at the austenite (γ) - ferrite (α) phase boundary, it can directly supply Mn for the austenite growth. Dislocation that ends at GBs can supply manganese to the GBs, which are faster diffusion channels (see table 2) and will facilitate further diffusion. Accordingly, dislocation migration is also expected to aid manganese diffusion, but study of this phenomena is out of the scope of current work.

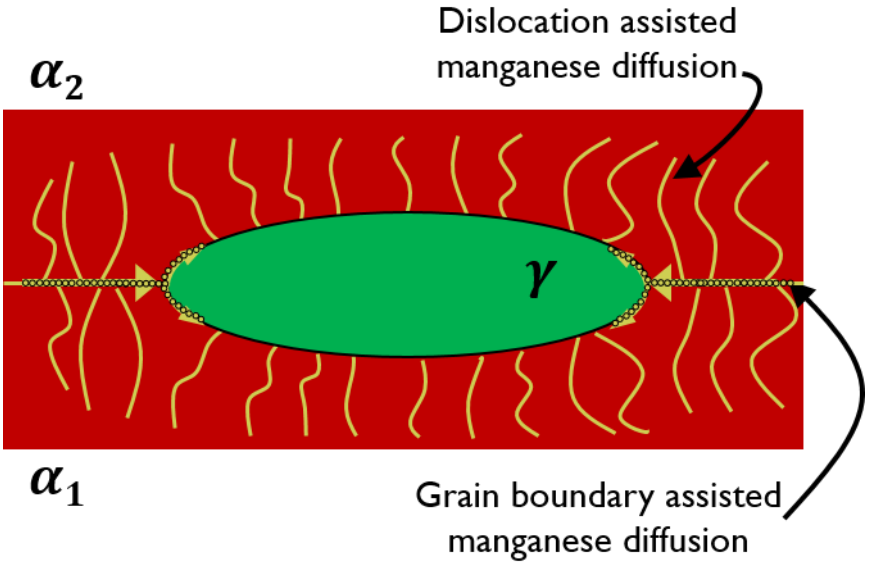

Figure 3 Schematic illustration of the manganese diffusion paths via grain/phase boundaries and dislocations. Dislocations terminating at the γ-α phase boundary can directly supply Mn for the austenite growth. Dislocations ending at α-α GB can supply Mn to the GB, which in turn acts as a faster diffusion pathway.

In line with earlier APT studies [6-9, 35, 36], we have also observed [37] manganese segregation to the GBs for the IA500/6. However, no direct evidence of GB diffusion and GB migration was observed from APT experiments for the IA500/6. To capture direct evidence of the GB diffusion and GB migration, our medium manganese steel was intercritically annealed at a lower temperature (slower manganese diffusivity) of 450°C for a shorter time of 2 hours (IA450/2).

Figure 4 illustrates the austenite(γ) nucleation event at a triple boundary in ferrite. Austenite volume is highlighted in figure 4a by a 30 at. % manganese iso-surface. The dotted line in the side view indicates the 2 nm thick cuboidal region of interest (ROI) (thickness perpendicular to the dotted line), located perpendicular to the ferrite α_1-α_2 GB, which was used to determine the two-dimensional (2-D) Mn-distribution and ion-density maps shown in figure 4b and figure 4c, respectively. It is important to note α-α GBs (indicated by red and black arrows in figure 4b and figure 4c), which are not clearly distinguishable in the Mn distribution map, are distinctly visible in the ion-density map figure 4c). One-dimensional (1-D) concentration profiles shown in figure 4d-f were calculated from cylindrical ROIs with 10 nm diameter and 0.5 nm bin width. The cylinder height is parallel to the arrows indicated on the respective schematic structure representations located above 1-D diagrams. One-dimensional (1-D) carbon concentration profiles corresponding to regions in figure 4d-f, are shown in supplementary (figure S3) to validate the absence of carbides.

Depletion of the Mn content was observed at the α-α GBs located in the vicinity of freshly grown austenite. It is particularly visible in 2-D Mn concentration map in figure 4 (b) and 1-D Mn-concentration profile across α_1-α_3 GB in figure 4 (f). This observation is counterintuitive, as typically, manganese segregation at the GB is expected and indeed, we observed in our study that the GB segregation of manganese in ferrite can be as high as ~43 at. % (see figure S4 in supplementary). Therefore, the GB manganese depletion observed in the austenite vicinity can be attributed to the Mn consumption by the growing austenite grain aided by fast diffusion of manganese along the GB.

In figure 4d, an asymmetric manganese distribution is observed across α_1-α_2 GB. Firstly, this finding validates that austenite nucleation and growth in cold rolled intercritically annealed medium manganese steels is a non-equilibrium process. While Kuzmina et al. [6] also found a similar skewed manganese distribution across a ferrite GB, it was attributed to plausible APT evaporation effects. However, Kuzmina et al. [6] did not observe any austenite in the analysed volume. Given that we observe growing austenite, we propose an alternative mechanism of GB migration. The stored deformation energy provides a driving force for GB migration [22] assisting in manganese diffusion as discussed earlier. The migration of the α_1-α_2 GB from grain α_2 towards α_1 can simultaneously supply manganese for austenite growth, thereby resulting in manganese depletion in the migrated region (α_2 grain in figures 4b and 4d). It is also important to note that no significant manganese segregation at the α_1-α_2 GB is present. As a consequence, the solute drag on the GB will be negligible, making it easier for the GB to migrate.

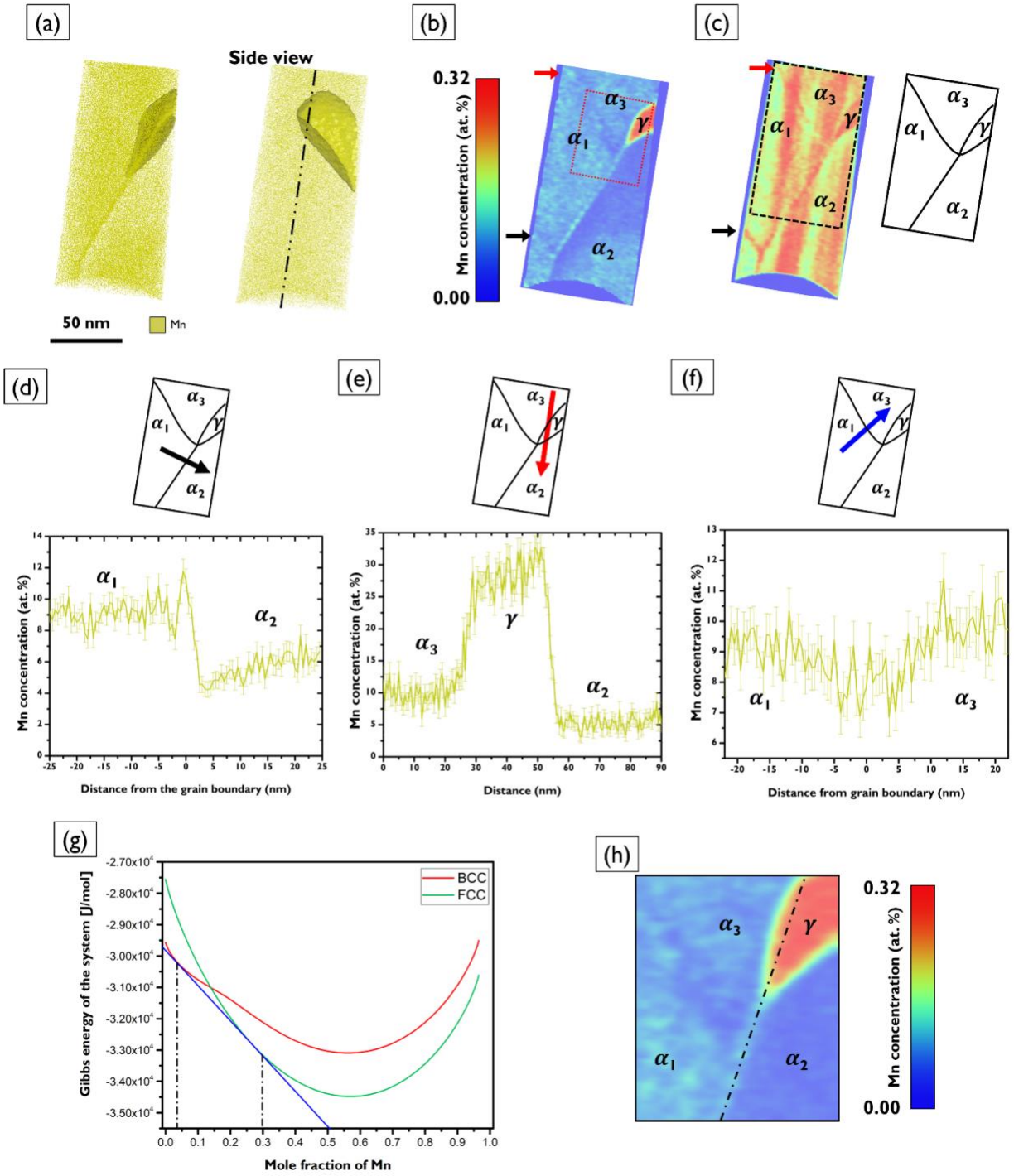

230

231 *Figure* ***Error! No text of specified style in document.*** *(a) Manganese elemental map for the IA450/2. The*
232 *austenite is highlighted with a 30 at. % Mn iso-surface. The dotted line in the side view corresponds to the 2nm*
233 *wide cuboidal ROI, which was used to determine the two dimensional (2-D) manganese distribution shown in (b)*
234 *and 2-D ion density map shown in (c). The GBs in ferrite are highlighted with a black and red arrow in (c). Further*
235 *a schematic of the austenite and ferrite grains (dotted box in 2-D ion density map) is also shown in (c). (d)*
236 *Asymmetric manganese distribution across ferrite(α_1)-ferrite(α_2) GB. The cylindrical region of interest is indicated in*
237 *figure 4a. (e) Manganese compositional profile across ferrite(α_3)-austenite(γ)-ferrite(α_2). The cylindrical region of*

interest is indicated with a red arrow in figure 4a. (f) Manganese depletion at the ferrite(α_1)-ferrite(α_3) GB. (g) Gibbs energy vs. mole fraction of manganese for the steel intercritically annealed at 450°C. (h) Inset from figure 4b (highlighted by a red dotted box) indicating preferential growth into the α_2 ferrite grain.

In the 1-D composition profile shown in figure 4e, adjacent to the phase boundary, the manganese concentration in ferrite grain α_3 is ~10 at. % but only ~4 at. % in grain α_2. Manganese is depleted in ferrite α_2 regions located near to the GB and the phase boundary. Nevertheless, in the area of grain α_2 located farther away from the GB and the phase boundary, the manganese composition reaches a level similar to that of ferrite grain α_3 (see figure 4b). The manganese concentration observed at the phase boundary in ferrite α_2 (~4 at. %) matches the equilibrium manganese concentration estimated at 450°C by thermodynamic calculations (plotted in figure 4g). Additionally, the austenite at the triple boundary grows preferentially into the α_2 ferrite grain. It is evident from the manganese 2-D elemental distribution in figure 4h that the austenite is protruding favorably into the α_2 ferrite grain. However, there is no significant growth of the austenite into the α_3 ferrite grain. This can be explained if the ferrite(α_3) - austenite (γ) interface is coherent while the ferrite (α_2) - austenite (γ) interface is incoherent. Formation of a coherent phase boundary (phase boundary with K-S orientation relationship) reduces the activation energy barrier for heterogeneous nucleation of austenite. The migration of such a coherent phase boundary (ferrite(α_3)-austenite) is interface controlled [38, 39]; therefore, low mobility is expected [38, 39]. On the contrary, the incoherent phase boundary with a non K-S orientation relationship (ferrite(α_2)-austenite) has higher energy and mobility, wherein the migration is diffusion controlled. Figure 5 is a schematic illustrating concentration profile of Mn across austenite-ferrite phase boundary for a coherent and incoherent interface. This also explains the manganese compositions observed in ferrite grain adjacent to the austenite. In a diffusion-controlled growth, the manganese composition in the ferrite adjacent to the interface equals the equilibrium manganese composition obtained from thermodynamic calculations (~4 at. % manganese in ferrite α_2 (figure 4e)). However, the manganese composition in ferrite at the phase boundary in an interface-controlled austenite growth equals the bulk ferrite composition (~10 at. % manganese in ferrite α_3 (figure 4e)).

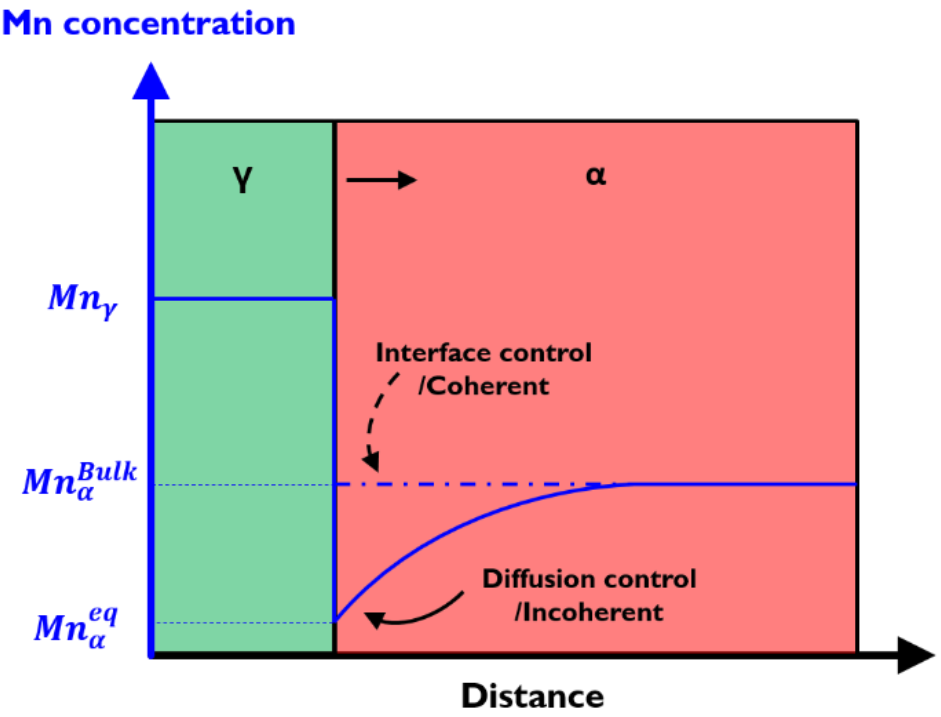

Figure 5: Schematic illustrating the manganese concentration across the austenite (γ)-ferrite (α) interface for a coherent and incoherent interface.

In summary, we showed that the GB diffusion, GB migration, and dislocation pipe diffusion play a prominent role in manganese transport for austenite growth during intercritical annealing. For the medium manganese steel annealed at 500°C for 6 hours (IA500/6), the grain size of austenite nucleated at HAGB is considerably greater (~25 times) compared to the austenite formed at a LAGB. This was attributed to the absence of bulk manganese diffusion and predominant GB diffusion, wherein the $D_{HAGB}^{Mn} > D_{LAGB}^{Mn}$ at 500°C. Direct evidence from APT experiments for GB diffusion and GB migration as manganese diffusion pathways for austenite growth has been shown for the IA450/2 specimen. Furthermore, we have shown the mobility and chemistry corresponding to coherent and incoherent austenite-ferrite phase boundaries.

Acknowledgments:

This work is funded by Tata Steel, IJmuiden, Netherlands, through IMPRS SURMAT scholarship. The authors thank Prof. Dierk Raabe for the discussions, and his inputs. The authors are grateful to Uwe Tezins, Christian Broß, and Andreas Sturm for their support to the FIB and APT facilities at MPIE.

References:

[1] Y. Mishin, C. Herzig, Materials Science and Engineering: A 260(1) (1999) 55-71.
[2] R.W. Balluffi, Journal of Electronic Materials 21(1) (1992) 527-553.
[3] S. Starikov, M. Mrovec, R. Drautz, Acta Materialia 188 (2020) 560-569.
[4] M. Mock, K. Albe, Journal of Nuclear Materials 509 (2018) 102-113.
[5] P. Kontis, Z. Li, D.M. Collins, J. Cormier, D. Raabe, B. Gault, Scripta Materialia 145 (2018) 76-80.
[6] M. Kuzmina, D. Ponge, D. Raabe, Acta Materialia 86 (2015) 182-192.
[7] A. Kwiatkowski Da Silva, R.D. Kamachali, D. Ponge, B. Gault, J. Neugebauer, D. Raabe, Acta Materialia 168 (2019) 109-120.
[8] Reza Darvishi Kamachali, Alisson Kwiatkowski da Silva, E. McEniry, D. Ponge, B. Gault, J. Neugebauer, D. Raabe, arXiv 1905.07970 (2019).
[9] J.T. Benzing, A. Kwiatkowski da Silva, L. Morsdorf, J. Bentley, D. Ponge, A. Dutta, J. Han, J.R. McBride, B. Van Leer, B. Gault, D. Raabe, J.E. Wittig, Acta Materialia 166 (2019) 512-530.
[10] E. Navara, B. Bengtsson, K.E. Easterling, Materials Science and Technology 2(12) (1986) 1196-1201.
[11] N. Nakada, K. Mizutani, T. Tsuchiyama, S. Takaki, Acta Materialia 65 (2014) 251-258.
[12] G. Gottstein, Physical Foundations of Materials Science, Springer Berlin Heidelberg, Berlin, Heidelberg, 2004, pp. 155-196.
[13] C. Herzig, Y. Mishin, in: P. Heitjans, J. Kärger (Eds.), Diffusion in Condensed Matter, Springer-Verlag, Berlin/Heidelberg, 2005, pp. 337-366.
[14] R.S. Varanasi, S. Zaefferer, B. Sun, D. Ponge, Materials Science and Engineering: A 824 (2021) 141816.
[15] K. Thompson, D. Lawrence, D.J. Larson, J.D. Olson, T.F. Kelly, B. Gorman, Ultramicroscopy 107(2-3) (2007) 131-9.
[16] M. Schaffer, B. Schaffer, Q. Ramasse, Ultramicroscopy 114 (2012) 62-71.
[17] A. Kovács, R. Schierholz, K. Tillmann, JLSRF 2 (2016) A43.
[18] Abhishek Tripathi, S. Zaefferer, arXiv:1906.10055v1 (2019).
[19] N. Mortazavi, M. Esmaily, M. Halvarsson, Materials Letters 147 (2015) 42-45.
[20] J. Liu, S. Lozano-Perez, A.J. Wilkinson, C.R.M. Grovenor, Ultramicroscopy 205 (2019) 5-12.
[21] L. Messina, M. Nastar, T. Garnier, C. Domain, P. Olsson, 90(10) (2014).
[22] A.L. Ruoff, R.W. Balluffi, Journal of Applied Physics 34(7) (1963) 1848-1853.
[23] J.R.G. Da Silva, R.B. McLellan, Materials Science and Engineering 26(1) (1976) 83-87.
[24] Y. Liu, L. Zhang, Y. Du, D. Yu, D. Liang, Calphad 33(3) (2009) 614-623.
[25] B. Zhang, AIP Advances 4(1) (2014) 017128.
[26] Y. Shima, Y. Ishikawa, H. Nitta, Y. Yamazaki, K. Mimura, M. Isshiki, Y. Iijima, MATERIALS TRANSACTIONS 43(2) (2002) 173-177.
[27] G. Gottstein, Springer Berlin Heidelberg2004, pp. 155-196.
[28] S. Chiesa, P.M. Derlet, S.L. Dudarev, H.V. Swygenhoven, Journal of Physics: Condensed Matter 23(20) (2011) 206001.
[29] H. Zhang, M.P.J. Punkkinen, B. Johansson, L. Vitos, Journal of Physics: Condensed Matter 22(27) (2010) 275402.
[30] B.B. He, B. Hu, H.W. Yen, G.J. Cheng, Z.K. Wang, H.W. Luo, M.X. Huang, Science 357(6355) (2017) 1029-1032.
[31] K. Lücke, K. Detert, Acta Metallurgica 5(11) (1957) 628-637.
[32] G. Gottstein, L.S. Shvindlerman, Grain Boundary Migration in Metals (2009).
[33] G. Gottstein, in: G. Gottstein (Ed.), Physical Foundations of Materials Science, Springer Berlin Heidelberg, Berlin, Heidelberg, 2004, pp. 303-356.
[34] O.C. Hellman, J.A. Vandenbroucke, J. Rüsing, D. Isheim, D.N. Seidman, Microsc. Microanal. 6(05) (2000) 437-444.
[35] M. `Kuzmina, M. Herbig, D. Ponge, S. Sandlobes, D. Raabe, Science 349(6252) (2015) 1080-1083.
[36] A. Kwiatkowski Da Silva, D. Ponge, Z. Peng, G. Inden, Y. Lu, A. Breen, B. Gault, D. Raabe, Nature Communications 9(1) (2018).
[37] R.S. Varanasi, Mechanisms of refinement and deformation of novel ultrafine-grained medium manganese steels with improved mechanical properties, Ruhr-Universität Bochum, Bochum, Germany, 2021.

335 [38] D.A. Porter, K.E. Easterling, K.E. Easterling, Phase Transformations in Metals and Alloys (Revised
336 Reprint), 0 ed., CRC Press2009.
337 [39] J. Mueller, D. Matlock, J. Speer, E. De Moor, Metals 9(9) (2019) 926.

338